

# RED-PSM: Regularization by Denoising of Partially Separable Models for Dynamic Imaging

Berk Iskender<sup>1\*</sup> Marc L. Klasky<sup>2</sup> Yoram Bresler<sup>1</sup>

<sup>1</sup>University of Illinois at Urbana-Champaign, IL, USA <sup>2</sup>Los Alamos National Laboratory, NM, USA

## Abstract

*Dynamic imaging addresses the recovery of a time-varying 2D or 3D object at each time instant using its undersampled measurements. In particular, in the case of dynamic tomography, only a single projection at a single view angle may be available at a time, making the problem severely ill-posed. In this work, we propose an approach, RED-PSM, which combines for the first time two powerful techniques to address this challenging imaging problem. The first, are partially separable models, which have been used to efficiently introduce a low-rank prior for the spatio-temporal object. The second is the recent Regularization by Denoising (RED), which provides a flexible framework to exploit the impressive performance of state-of-the-art image denoising algorithms, for various inverse problems. We propose a partially separable objective with RED and an optimization scheme with variable splitting and ADMM, and prove convergence of our objective to a value corresponding to a stationary point satisfying the first order optimality conditions. Convergence is accelerated by a particular projection-domain-based initialization. We demonstrate the performance and computational improvements of our proposed RED-PSM with a learned image denoiser by comparing it to a recent deep-prior-based method TD-DIP.*

## 1. Introduction

Time-varying tomography is a challenging ill-posed inverse problem that involves reconstructing a dynamic object using its sequential projections at each time instant. Since the measurements are inconsistent due to the evolving object, traditional reconstruction algorithms lead to significant artifacts.

The problem arises in microscopic tomography [18], myocardial perfusion imaging [5], imaging of fluid flow processes [19, 29] and dynamic imaging of material samples undergoing compression [21, 22]. Also, it is closely

related to the dynamic MRI problem, which typically arises in cardiac imaging [28].

Previous work [32, 33] includes treating the problem as a time-sequential sampling problem of bandlimited signals and provides an optimal view angle order for the scan. Despite providing theoretical guarantees for unique and stable reconstruction, the approach is limited by its bandlimitedness assumptions.

Several methods [26, 34] recover the underlying motion field from projections using the Radon transform properties. However, these methods require the object information a priori. Other algorithms [13, 14] alternate between estimating the motion field and the time-varying object. These methods assume the total density to be preserved for a given object at different times which may be a limiting assumption. For instance, imaging a fixed slice of a time-varying object under compression may violate this assumption due to perpendicularly evolving parts.

In dynamic tomography and MRI, partially-separable models (PSM) have been used to represent the underlying object [10] and the time-sequential projections [11, 12]. The Projection-domain PSM in [11, 12] carries the PSM to the projection domain using the harmonic representation of projections, and provides uniqueness and stability analysis for the problem. In spite of this advantage of the projection domain PSM over its object-domain counterparts, the performance of this approach is limited by the null space of the measurement operator. A different PSM-based method for dynamic MRI [38] imposes the low-rank structure as a soft-constraint. It uses a hybrid objective with the PSM model used in the data fidelity term and the object in a simple  $l_1$ -norm penalty, with an additional penalty term to penalize the mismatch between the PSM and the object. The method does not use a guided initial guess for the object or for the PSM basis functions.

Recently, object-domain deep image prior (DIP)-based algorithms [36, 40] have been proposed for dynamic MRI. Providing impressive results, DIP-based algorithms such as [36] suffer from overfitting and usually require handcrafted early stopping criteria during the optimization of generator network parameters. In an attempt to overcome the overfit-

\*Corresponding email: berki2@illinois.edu

This research was supported in part by Los Alamos National Labs under Subcontract No. 599416/CW13995.

ting and the need for handcrafted early stopping, the authors of [40] regularize the problem by constraining the geodesic distances between generated objects in proportion to the distances between their latent representation. However, this requires the computation of the Jacobian of the generator network at each iteration of the update of the weights and significantly increases the computational load and run time.

A different approach [3] combines partially separable and generative models. It employs spatial and temporal regularization by penalizing the generator weights and a particular initialization scheme for the inputs to the generator networks. Although it combines the PSM with the recent DIP framework, this method has the following limitations, which are overcome by the proposed approach: (i) The spatial generator is an artifact removal network taking the full-sized spatial basis functions as input. Since this prevents a patch-based implementation, it may be computationally problematic for high-resolution 3D+temporal settings. (ii) The CNN prior for natural images may not be useful as a prior for the individual spatial basis functions, since the least-squares optimal spatial basis functions are the left singular vectors of the complete object, and as such may not have the structure of natural images. (iii) As with the other DIP-based methods, if the additional penalty on the generator parameters is insufficient, this method can be prone to overfitting.

#### Contributions

1. To the best of our knowledge, RED-PSM is the first PSM-based approach to dynamic imaging, that uses a pre-trained, learned (RED-based [27]) spatial prior.
2. A novel and effective ADMM algorithm for the resulting new minimization problem enforcing PSM as a hard constraint is proposed
3. The method is supported by theoretical analysis, with a convergence guarantee.
4. Compared to a recent DIP-based [36] algorithm, RED-PSM achieves better reconstruction accuracy with orders of magnitude faster run times.
5. A version of the approach with a patch-based regularizer is shown to provide almost equivalent reconstruction accuracy. This makes the proposed method conveniently scalable to high-resolution 3D or 4D settings.

## 2. Problem Statement

In a 2D setting, the goal in the ill-posed dynamic tomography problem is to reconstruct a time-varying object  $f(\mathbf{x}, t)$ ,  $\mathbf{x} \in \mathbb{R}^2$  vanishing outside a disc of diameter  $D$ , from its projections

$$g(s, \theta, t) = \mathcal{R}_\theta \{f(\mathbf{x}, t)\}$$

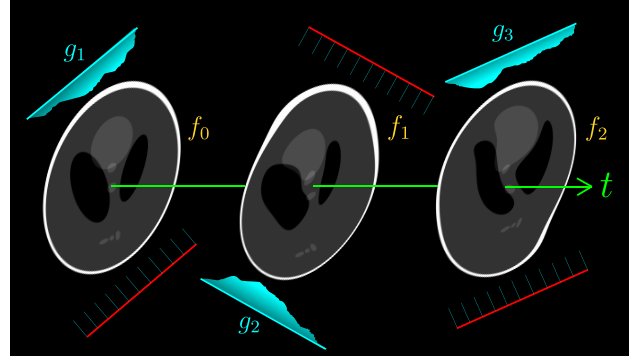


Figure 1: Projection acquisition geometry for time-varying tomography of the object  $f_t$  with single measurement  $g_t$  at each time instant for  $t \in \{0, 1, 2\}$ .

obtained using the Radon transform operator  $\mathcal{R}_\theta$  at angle  $\theta$ . Considering time-sequential sampling, in which only one projection is acquired at each time instant, and sampling uniform in time, the acquired measurements are

$$\{g(s, \theta_p, t_p)\}_{p=0}^{P-1}, \quad \forall s, t_p = p\Delta_t, \quad (1)$$

where  $s$  is the offset of the line of integration from the origin (i.e., detector position), and  $P$  is the total number of projections (and temporal samples) acquired. The sampling of the  $s$  variable is assumed fine enough and is suppressed in the notation. The angular sampling scheme, the sequence  $\{\theta_p\}_{p=0}^{P-1}$ , with  $\theta_p \in [0, 2\pi]$ , is considered as a free design parameter. Figure 1 shows a simplified time-sequential sampling scheme for a time-varying object.

Our objective in dynamic tomography is to reconstruct the underlying object with temporal variation  $\{f(\mathbf{x}, t_p)\}_{p=0}^{P-1}$  from the time-sequential projections in (1). The challenge is that because each projection belongs to a different object, the projections in (1) are inconsistent. Therefore, a conventional, e.g., filtered backprojection (FBP) reconstruction as for a static object results in significant reconstruction artifacts.

## 3. Partially Separable Models (PSM)

For spatio-temporal inverse problems such as dynamic MRI and tomography, the underlying object can be accurately represented using a partially-separable model (PSM), which effectively introduces a low-rank prior to the problem. For dynamic tomography, a PSM can represent the imaged object  $f$ , or its full set of projections  $g$ . In this paper we use an object-domain PSM.

The representation of a dynamic object  $f(\mathbf{x}, t)$  by a  $K$ -th order partially separable model (PSM) is the series expansion

$$f(\mathbf{x}, t) = \sum_{k=0}^{K-1} \Lambda_k(\mathbf{x}) \psi_k(t). \quad (2)$$

The model helps with interpretability by separating the spatial structure from the temporal dynamics. This expansion is dense in  $\mathcal{L}_2$  [2], meaning that any finite energy object can be approximated arbitrarily well by such a model of sufficiently high order. Empirically, modest values of  $K$  provide high accuracy in applications to MR cardiac imaging [10, 16, 17]. Theoretical analysis in [12] shows that for a spatially bandlimited object undergoing a time-varying affine transformation (i.e., combination of time-varying translation, scaling, and rotation) of bounded magnitude, a low order PSM provides a good approximation.

The PSM for the object using a  $d$ -dimensional representation for the temporal functions leads to significant reduction of  $\approx PD^2$  representation parameters for an unstructured object of diameter  $D$  with  $P$  temporal samples to  $\approx KD^2 + Kd$  with  $K \ll P$  and  $d \ll P$ . Thus, it provides an effective parsimonious model for the spatio-temporal object  $f$ .

Also, by propagating the PSM object model to the projection domain, it enables quantitative analysis [12] of the choice of optimal sequential projection angular schedule.

## 4. Proposed Method: RED-PSM

### 4.1. Variational Formulation

We use a discretized version of the PSM (2) for the dynamic object, with the object  $f(\cdot, t)$  at each time instant  $t = 0, 1, \dots, P-1$ , represented by a  $J \times J$ -pixel image. Vectorizing these images to vectors  $f_t \in \mathbb{R}^{J^2}$ , the entire dynamic object is the  $J^2 \times P$  matrix  $f = [f_0 \dots f_{P-1}] = \Lambda \Psi^T \in \mathbb{R}^{J^2 \times P}$ . The columns  $\Lambda_k$  and  $\Psi_k$  of  $\Lambda \in \mathbb{R}^{J^2 \times K}$  and  $\Psi \in \mathbb{R}^{P \times K}$  are the discretized spatial and temporal basis functions for the PSM representation, respectively.

Assuming that the x-ray detector has  $J$  bins, the projection of the object at time  $t$  is  $g_t = g(\cdot, \theta_t, t) = R_{\theta_t} f_t \in \mathbb{R}^J$ , where the measurement matrix  $R_{\theta_t} \in \mathbb{R}^{J \times J^2}$  computes the projection at view angle  $\theta_t$ .

We formulate the recovery of  $f$  as the solution  $\hat{f} = \hat{\Lambda} \hat{\Psi}^T$  to the following variational problem

$$(\hat{\Lambda}, \hat{\Psi}) = \arg \min_{\Lambda, \Psi} \sum_{t=0}^{P-1} \|R_{\theta_t} (\sum_{k=0}^{K-1} \Lambda_k \psi_k[t]) - g_t\|_2^2 + \lambda D(\Lambda \Psi^T) + \xi \|\Psi\|_F^2 \quad \text{s.t.} \quad \Psi = UZ. \quad (3)$$

The first term is the data fidelity term measuring the fit between available undersampled measurements  $g_t$  of the true object and the measurements obtained from the estimated object  $f = \Lambda \Psi^T \in \mathbb{R}^{J^2 \times P}$ .

The second term  $D(\Lambda \Psi^T)$  with weight  $\lambda > 0$  is a *spatial* regularizer injecting relevant spatial prior to the problem. The third term with weight  $\xi > 0$  is a simple two-norm penalty on the temporal basis functions. This penalty

prevents one of the bilinear factors  $\Lambda$  or  $\Psi$  from growing without limit, while the other shrinks to zero.

Finally, the constraint  $\Psi = UZ$  is an implicit *temporal* regularizer that restricts the temporal basis functions  $\Psi$  to a  $d$ -dimensional subspace of  $\mathbb{R}^P$  spanned by a fixed interpolator  $U \in \mathbb{R}^{P \times d}$ . In practice, we incorporate this constraint by explicit substitution (reparametrization of  $\Psi$  in terms of the free variable  $Z \in \mathbb{Z}^{d \times K}$ ) into the objective, and the minimization in (3) over  $\Psi$  is thus replaced by minimization over  $Z$ . This reduces the number of degrees of freedom in  $\Psi$  to a fixed number  $dK$ , independent of the number  $P$  of temporal sampling instants. For notational conciseness, We do not display this constraint/reparametrization in the sequel, but it is used throughout.

### 4.2. Incorporating Regularization by Denoising

For the spatial regularizer  $D(\cdot)$  we consider ‘‘Regularization by Denoising (RED)’’ [27]. RED proposes a recovery method using a denoiser in an explicit regularizer of the form

$$D(f) = \frac{1}{2} f^T (f - G(f)) \quad (4)$$

where  $G : \mathbb{R}^{J^2} \rightarrow \mathbb{R}^{J^2}$  is the denoising operator. Providing significant flexibility for the type of denoisers that can be used, RED still requires  $G$  to be differentiable and locally homogeneous, and to satisfy the passivity condition  $\|G(f)\| \leq \|f\|$ .<sup>1</sup>

For the conventional variational formulation

$$\hat{f} = \arg \min_f \sum_{t=0}^{P-1} \|R_{\theta_t} f_t - g_t\|_2^2 + \lambda D(f),$$

an efficient choice are iterative algorithms [27] that use the standard ‘‘early termination’’ approach [4], and only require a single use of the denoiser per iteration.

However, the regularized PSM objective in (3) does not allow to propagate the RED updates on  $f$  to the respective basis functions in an efficient manner. To overcome this difficulty, we perform a bilinear variable splitting  $f = \Lambda \Psi^T$  and obtain our final formulation

$$\min_{f, \{\Lambda_k\}, \{\psi_k\}} \sum_t \|R_{\theta_t} (\sum_k \Lambda_k \psi_k[t]) - g_t\|_2^2 + \lambda D(f) + \xi \|\Psi\|_F^2 \quad \text{s.t.} \quad f = \Lambda \Psi^T. \quad (5)$$

Since the PSM is enforced as a hard constraint, the estimated object  $f$  is constrained to have  $\text{rank}(f) \leq K$ . We propose an algorithm based on ADMM to solve (5).

<sup>1</sup>While many powerful denoisers have been demonstrated [27] to satisfy these conditions, recent work [25] provides an alternative framework to explain the good performance of RED with denoisers not satisfying conditions in [27].

To cast the problem with the PSM constraint into the ADMM framework, we form the augmented Lagrangian, [7, 8]

$$\mathcal{L}_\beta(\Lambda, \Psi, f, \gamma) = \sum_t \|R_{\theta_t}(\sum_k \Lambda_k \psi_k[t]) - g_t\|_2^2 + \lambda D(f) + \xi \|\Psi\|_F^2 - \frac{1}{2\beta} \|\gamma\|_F^2 + \frac{\beta}{2} \|\Lambda \Psi^T - f + \frac{1}{\beta} \gamma\|_F^2, \quad (6)$$

where  $\gamma \in \mathbb{R}^{P \times J^2}$  represents the dual variable and  $\beta > 0$  is the penalty parameter.

Then, the ADMM can be used to solve (6) as in Algorithm 1.

---

**Algorithm 1** PSM-ADMM

---

**input:**  $\Lambda^{(0)}, \Psi^{(0)}, \gamma^{(0)}, f^{(0)} = \Lambda^{(0)} \Psi^{(0)T}, \beta > 0, \lambda > 0, \xi > 0$

- 1: **for**  $i \in \{1, \dots, I\}$  **do**
- 2:  $\Lambda^{(i)}, \Psi^{(i)} = \arg \min_{\{\Lambda_k\}, \{\psi_k\}} \{ \sum_t \|R_{\theta_t}(\sum_k \Lambda_k \psi_k[t]) - g_t\|_2^2 + \frac{\beta}{2} \|\Lambda \Psi^T - f^{(i-1)} + \frac{1}{\beta} \gamma^{(i-1)}\|_F^2 + \xi \|\Psi\|_F^2 \}$
- 3:  $f^{(i)} = \arg \min_f \{ \lambda D(f) + \frac{\beta}{2} \|\Lambda^{(i)} \Psi^{(i)T} - f + \frac{1}{\beta} \gamma^{(i-1)}\|_F^2 \}$
- 4:  $\gamma^{(i)} = \gamma^{(i-1)} + \beta (\Lambda^{(i)} \Psi^{(i)T} - f^{(i)})$
- 5: **end for**

---

Line 3 in Algorithm 1 corresponds to the variational denoising of  $\Lambda^{(i)} \Psi^{(i)T} + \gamma^{(i-1)}$  with regularization  $\lambda D(f)$ . Algorithm 1 is reformulated into Algorithm 2 to use RED as in [27] and [25], where  $G_\phi$  is the denoiser for which we have the gradient rule

$$\nabla D(f) = f - G_\phi(f) \quad (7)$$

and the  $f$  update in Step 4 is a single fixed-point iteration step using the approach of early stopping [4] (Sec. 4.3.2). In contrast to an iterative method to perform Line 3 in Algorithm 1, Step 4 in Algorithm 2 requires only single use of the denoiser per iteration of ADMM.

### 4.3. Regularization Denoiser

The regularization denoiser  $G_\phi$  has a DnCNN [37] architecture and was trained in a supervised manner on a training set of *static* 2D slices  $f_i \in \mathbb{R}^{J^2}, i = 1, \dots, N$  assuming that such data will be available in the settings of interest. Thus, the RED steps are agnostic to the specific motion type. The training objective for the denoiser is

$$\min_{\phi} \sum_i \|f_i - G_\phi(\tilde{f}_i)\|_F^2 \quad s.t. \quad \tilde{f}_i = f_i + \eta_i, \forall i, \quad (8)$$

where the injected noise  $\eta_i \sim \mathcal{N}(0, \sigma_i^2 I)$  has noise level  $\sigma_i \sim U[0, \sigma_{\max}]$  spanning a range of values, so that the denoiser learns to denoise data with various noise levels.

---

**Algorithm 2** RED-PSM-ADMM

---

**input:**  $\Lambda^{(0)}, \Psi^{(0)}, \gamma^{(0)}, f^{(0)} = \Lambda^{(0)} \Psi^{(0)T}, \beta > 0, \lambda > 0, \xi > 0$

- 1: **for**  $i \in \{1, \dots, I\}$  **do**
- 2:  $\Lambda^{(i)} = \arg \min_{\Lambda} \{ \sum_t \|R_{\theta_t}(\sum_k \Lambda_k \psi_k^{(i-1)}[t]) - g_t\|_2^2 + \frac{\beta}{2} \|\Lambda \Psi^{(i-1)T} - f^{(i-1)} + \frac{1}{\beta} \gamma^{(i-1)}\|_F^2 \}$
- 3:  $\Psi^{(i)} = \arg \min_{\Psi} \{ \sum_t \|R_{\theta_t}(\sum_k \Lambda_k^{(i)} \psi_k[t]) - g_t\|_2^2 + \frac{\beta}{2} \|\Lambda^{(i)} \Psi^T - f^{(i-1)} + \frac{1}{\beta} \gamma^{(i-1)}\|_F^2 + \xi \|\Psi\|_F^2 \}$
- 4:  $f^{(i)} = \frac{\lambda}{\lambda + \beta} G_\phi(f^{(i-1)}) + \frac{\beta}{\lambda + \beta} (\Lambda^{(i)} \Psi^{(i)T} + \frac{1}{\beta} \gamma^{(i-1)})$
- 5:  $\gamma^{(i)} = \gamma^{(i-1)} + \beta (\Lambda^{(i)} \Psi^{(i)T} - f^{(i)})$
- 6: **end for**

---

### 4.4. Convergence Analysis

In Appendix C, we follow an approach along the lines of [9] to analyze convergence. We show that under mild technical conditions, the objective in a close variant of Algorithm 2 is guaranteed to converge (with increasing number  $I$  of iterations) to a value corresponding to a stationary point of the Lagrangian, that is, satisfying the necessary conditions for first order optimality. In practice, the version we implemented and used in the experiments reported in Section 5 has better run times, and rapid empirical convergence.

## 5. Experiments

### 5.1. Datasets

Two categories of data sets are used in this work.

*Walnut Dataset:* We use the CT reconstructions of two different (static) walnut objects from the publicly available 3D walnut CT dataset [6]. We create a dynamic test object by synthetically warping the central axial slice of one of the walnut objects using a sinusoidal piecewise-affine time-varying warp [1]. To be precise, the image is divided into a  $J \times J$  uniformly spaced rectangular grid, and the following vertical displacement is applied on each row separately to drive the temporally varying warp  $\Delta_{j,t} = -C(t) \sin(3\pi j/J), j \in \{0, \dots, J-1\}$ , where  $C(t)$  is a linearly increasing function of  $t$  and  $C(0) = 0$ . *Static* axial, coronal, and sagittal slices of the other walnut object are used to train the denoiser  $G_\phi$ .

*Compressed Object Dataset:* The compressed object data set is obtained from a materials science experiment [20] with a sequence of nine increasing compression steps applied to an object, with a full set of radiographic projections collected (using Carl Zeiss Xradia 520 Versa) and reconstructed by the instrument’s software at each step. Using this quasi-static data set, a fixed axial slice is extracted from each reconstruction. Nine extracted slices are interpolated

to  $P$  time frames using a recent deep learning-based video interpolation algorithm [24]. The denoiser  $G_\phi$  for our experiments on this data set was trained using the axial slices of the *static* pre-compression and post-compression objects.

We note that all algorithms compared in this paper are agnostic to both the synthetic warp applied on the static walnut slice and to the data-driven interpolation method used for the compressed object.

Spatio-temporal projection data for each dataset is simulated by a parallel-beam projection with  $J = 128$  detector bins of the dynamic phantoms, a single projection at each of the  $P$  time instants. The sequence of projection angles  $\{\theta_t\}_{t=0}^{P-1}$  (a free experimental design parameter) was chosen to follow the bit-reversed view angle sampling scheme, which has been shown [11] to provide an especially favorable conditioning of the recovery problem. The simulated measurements are corrupted using AWGN with standard deviation  $\sigma = 5 \cdot 10^{-3}$ . This noise level leads to the FBP (with Ram-Lak filter) of the full set of  $P = 512$  *projections at each time instant* having a PSNR of approximately 46 dB. When, in the actual experiments with sequentially sampled data, only  $1/P$  of this data is used, the PSNR of the reconstruction may be expected to be lower.

Ground-truth frames for each dataset for  $P = 8$  are shown in Figure 2.

## 5.2. Baseline Methods

**PSM-TV:** Similar to the proposed approach, this algorithm also uses a partially separable model to represent the object with a different regularization type. For PSM-TV, regularization penalizes the  $\ell_1$ -norm of the discrete 2D total variation of the temporal slices of  $f$  at each time instant. To this end, the constraint  $f = \Lambda\Psi^T$  is implemented by substitution into the objective in (5), and the definition of  $D$  is changed to

$$D(\Lambda\Psi^T) = \sum_t \text{TV}((\Lambda\Psi^T)[\cdot, t]), \quad (9)$$

and the rest of the objective is kept the same. The unconstrained problem is then solved for  $\{\hat{\Lambda}, \hat{\Psi}\}$  (using, as a convenient implementation, the Adam optimizer in Pytorch). Finally, the estimated object is obtained as  $\hat{f} = \hat{\Lambda}\hat{\Psi}^T$ .

**TD-DIP [36]:** TD-DIP is a recent method based on the Deep Image Prior (DIP) approach.<sup>2</sup> It uses a mapping network  $M_\alpha$  and a generative model  $N_\beta$  sequentially to obtain the estimated object at each time instant  $f_t$  from fixed and handcrafted latent representations  $\xi_t$ . Because TD-DIP was

<sup>2</sup>It would be interesting to include yet another baseline method – the DIP-based PSM approach [3] (also developed for MRI). However we were unable to do so as an implementation of this method was not available, and because of potential issues (due to specific initialization and framework that use other MRI-targeted algorithms) with replicating its performance and adapting to our CT problem.

originally proposed for dynamic MRI, we modified the objective minimally for dynamic tomography as

$$\min_{\alpha, \beta} \sum_t \|g_t - R_{\theta(t)}((N_\beta \circ M_\alpha)(\xi_t))\|^2. \quad (10)$$

For the comparisons in this work, identical mapping network and generator architectures, latent representation dimensionality, optimizer, learning rate, and decay schemes are used as in the available online implementation [35]. The original work focuses on the beating heart problem and thus proposes a helix-shaped latent manifold for  $\xi_t$  with cycles equal to the number of heartbeats during measurement acquisition. Since we do not have a repetition assumption for the motion types included in this paper, we use a linear manifold as explained in the original paper [36]. Thus, the method is sometimes denoted as “TD-DIP (L)” in Section 5.4 for clarification.

## 5.3. Experimental Settings

All methods are run on a workstation with an Intel(R) Xeon(R) Gold 5320 CPU and NVIDIA RTX A6000 GPU. In practice, we used a minor variation of Algorithm 2, where we combined the subproblems in Lines 2 and 3, and minimized with respect to both basis functions simultaneously using gradient descent with Adam [15] optimizer.

**Denoiser training.** The upper limit for noise level used in training the denoiser was set to  $\sigma_{\max} = 5 \cdot 10^{-2}$ . For the dynamic walnut object, the denoiser  $G_\phi$  is trained on the central 200 axial, 200 sagittal, and 200 coronal slices of another walnut CT reconstruction downsampled to size  $128 \times 128$ . For the compressed object, axial slices of pre-compression and post-compression *static* objects, containing 462 slices in total, are used to train  $G_\phi$ . For both datasets,  $G_\phi$  is trained for 500 epochs using the Adam optimizer with a learning rate of  $5 \cdot 10^{-3}$ . Each convolutional layer is followed by a ReLU nonlinearity except for the final layer, which has a single-channel output. We test both direct and residual DnCNN denoisers where the former predicts the denoised image and the latter estimates the noise from the noisy input.

Architectural details for denoisers used in our experiments are provided in Table 5 in Appendix B. We use a fixed pre-trained denoiser for all  $P$  for the same object type.

**Temporal interpolation.** In all experiments, we use a cubic spline interpolator for  $U$ , to interpolate the low-dimensional temporal representation  $Z$  to  $\Psi$ .

**Initialization.** Unless stated otherwise, the first  $K$  spatial and temporal basis functions are initialized using the SVD truncated to order  $K$  of the dynamic object estimate produced by a recent projection-domain PSM-based method called “ProSep” [12]. Otherwise, the spatial basis functions are initialized as 0 and the latent representations



Figure 2: Ground-truth frames for the time-varying walnut (top) and compressed object (bottom) datasets, uniformly sampled in time,  $t \in \{0, \dots, P - 1\}$ , for  $P = 8$ .

$z_k$  of the temporal basis functions are initialized randomly as  $z_k \sim \mathcal{N}(0, I)$ .

**Tomographic Acquisition Scheme.** All methods mentioned in this paper use the bit-reversed angular sampling scheme, over the range  $[0, \pi]$ .

**Run Times.** For  $P = 256$  and using the specified computational resources and parameter settings, RED-PSM-ADMM with ProSep initialization requires  $50 < \text{steps} < 150$  taking about 2 to 6 minutes whereas TD-DIP with batch size  $P$  typically requires  $> 30k$  steps, taking about 3.5 hours to complete. Hence, RED-PSM provides a speedup over TD-DIP by a factor of 35 to 105 to reach its peak performance. We note that based on the parameter configuration, the speedup factor may vary. However, the proposed method provides a significant run time reduction in all cases.

**Evaluation Metrics.** Four quantitative metrics were implemented for comparing different method performances. These metrics are; (i) the *peak signal-to-noise ratio* (PSNR) in dB, (ii) the *structural similarity index* (SSIM) [31], (iii) the *mean absolute error* (MAE), and (iv) the *high-frequency error norm* (HFEN) [23] defined as

$$\text{HFEN}(f, f_r) = \|\text{LoG}(f) - \text{LoG}(f_r)\|_2 \quad (11)$$

where LoG is a rotationally symmetric Laplacian of Gaussian filter with a standard deviation of 1.5 pixels.

## 5.4. Results

### 5.4.1 Reconstruction accuracies for different $P$

In Figure 5 and Table 1, the performance of the RED-PSM-ADMM with different initialization techniques is compared with PSM-TV and TD-DIP with linear latent representation for both objects. For various  $P$ , the proposed algorithm performs on par with or better than TD-DIP in terms of PSNR. The PSNR improvement for RED-PSM enhances with the increase in  $P$ . Moreover, the improvement with RED-PSM is more significant when SSIM, MAE, and HFEN are considered.

Figure 3 compares the reconstructions for both objects at two different  $t$  for  $P = 256$ . As expected, PSM-TV performs the worst among the compared methods and provides blurry reconstructions which lack finer details for both objects. TD-DIP reconstructions contain visible noise-like artifacts on the piecewise constant regions of the walnut object, which are alleviated by RED-PSM. This observation manifests itself also in the absolute difference figures with a more uniformly distributed error map for TD-DIP at the interior regions of the walnut. Also, RED-PSM is further able to preserve sharper details around the shell of the walnut. For the compressed material, we also see an almost uniformly increased absolute error over the object for the given time frames for TD-DIP compared to RED-PSM. This difference becomes further distinguishable around the highly dynamic regions of the object, emphasizing the advantage of the proposed method.

In Figure 4, the reconstructed  $x$ - $t$  cross sections of the dynamic walnut are shown for different methods. The location of the cross-section is highlighted by a yellow line on the static  $x$ - $y$  frame at  $t = 0$ . Consistent with the comparison in Figure 3, RED-PSM leads to reduced absolute error values throughout the respective cross-section. Also, TD-DIP leads to higher background errors. This is easier to inspect on the error figures.

### 5.4.2 Effect of Initialization

The initialization of  $\Lambda$ ,  $\Psi$ , and  $f$  plays an important role in the performance and convergence speed of RED-PSM. We observe significant speed-up when rather than a random initialization, we initialize the algorithm with ProSep [11] estimated reconstruction. Figure 6 shows PSNR vs. iterations comparison for different initialization techniques for the dynamic walnut object with  $P = 256$ . The rest of the parameters were selected identically as indicated in Table 3. This experiment highlights the advantages of initializing with ProSep estimated basis functions: eliminating the need for multiple runs for a best-case result; and speeding up convergence considerably.

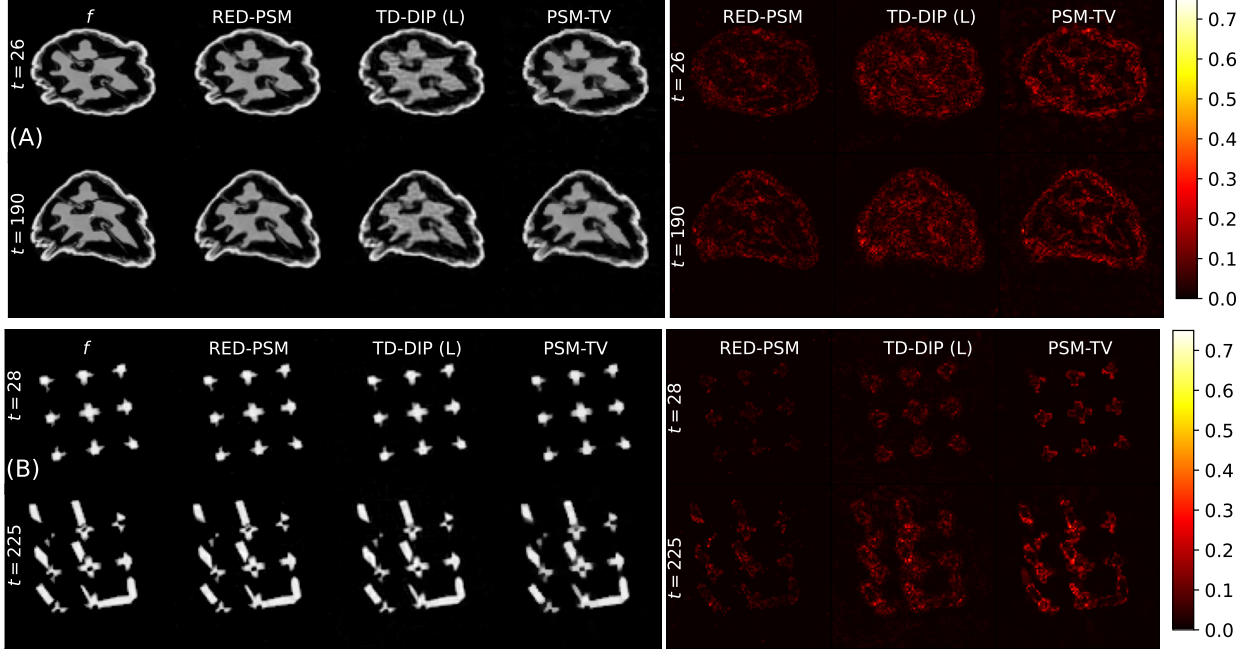


Figure 3: Comparison of two reconstructed temporal slices (left) and the corresponding normalized absolute residual images (right) for (A) the time-varying walnut, and (B) compressed object using different methods for  $P = 256$ .

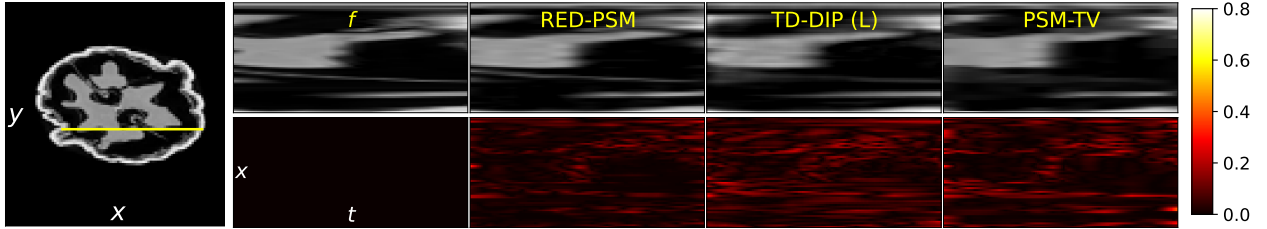


Figure 4: Comparison of reconstructed  $x$ - $t$  cross-sections using different methods for  $P = 256$ . The location of the cross-section is indicated with a yellow line on the static object at time  $t = 0$  (left). These cross-sections (top) are provided with the normalized absolute error counterparts (bottom). The  $x$ - $y$ - $t$  dimensions are indicated on the static object and bottom left absolute error figure in white text for reference.

### 5.4.3 Patch-based RED denoiser

To improve the scalability of the method to higher resolution and/or 3D dynamic objects conveniently, the objective in (5) can be manipulated to operate on the patches of temporal slices of the time-varying object to circumvent the need to store the complete object  $f$  in the memory. This requires the denoiser  $G_\phi$  to operate on the patches of temporal instances. To showcase the potential of the suggested scheme, we replace the full-size image denoiser with a patch-based counterpart in the RED step and compare the performance with the originally proposed method for 2D dynamic objects.

The patch-based denoiser for RED updates is trained us-

ing

$$\min_{\phi} \sum_i \sum_l \|B_l f_i - G_\phi(B_l \tilde{f}_i)\|_F^2 \text{ s.t. } \tilde{f}_i = f_i + \eta_i, \forall i, \quad (12)$$

where  $\eta_i, \sigma_i$  are set as in (8), and  $B_l$ , with  $l \in \{0, \dots, L-1\}$ , is the operator to extract the  $l$ -th patch of the image. The denoiser  $G_\phi$  operates separately on each patch.

To train the patch-based denoiser, uniformly random rotations (multiples of  $\pi/2$ ), and random horizontal/vertical flips, each with a probability of 1/2, were used for data augmentation.

Table 2 shows that both denoiser types perform similarly using the same denoiser training policy as described in Section 5.3 for both objects, confirming the effectiveness of the



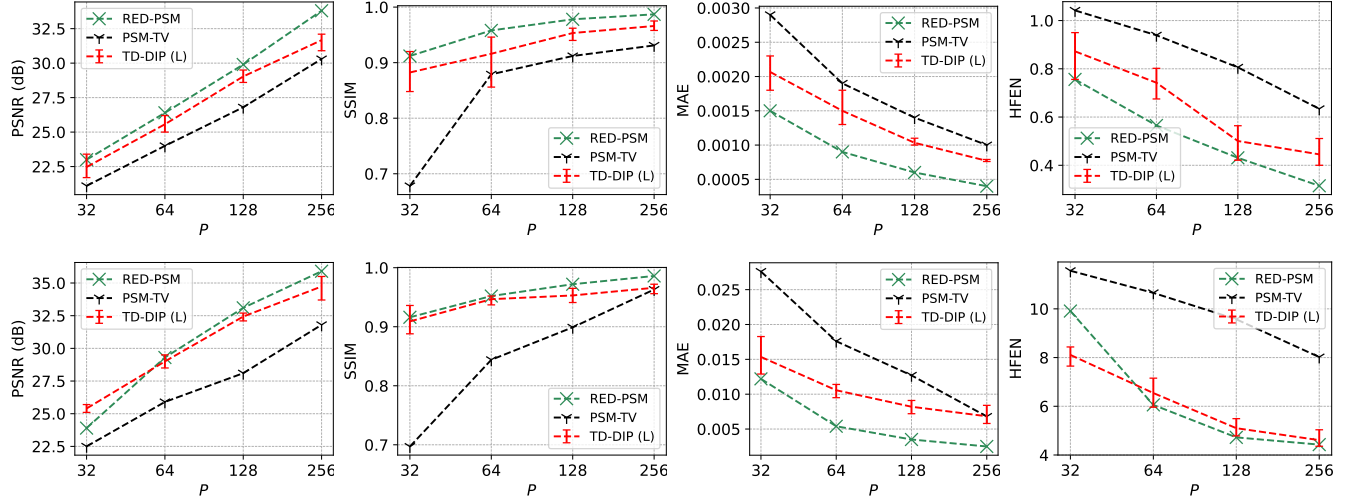


Figure 5: Reconstruction PSNR, SSIM, MAE, and HFEN for the time-varying walnut object (top) and compressed material (bottom) vs.  $P$  using different methods. For TD-DIP, accuracy statistics for the best PSNR reconstruction during optimization are reported assuming such an oracle is available. The minimum and maximum values are indicated with error bars and the mean values are connected by the dashed line for different  $P$  for three different runs.

		(a) Walnut				(b) Compressed Material			
$P$	Method	PSNR(dB)	SSIM	MAE	HFEN	PSNR(dB)	SSIM	MAE	HFEN
32	PSM-TV (R)	21.1	0.678	0.0029	1.042	22.5	0.697	0.0286	11.564
32	TD-DIP (L)	22.5	0.882	0.0021	0.872	25.4	0.909	0.0149	8.109
32	RED-PSM-ADMM (P)	22.7	0.914	0.0015	0.789	23.9	0.916	0.0122	9.910
64	PSM-TV (R)	24.0	0.879	0.0019	0.939	25.6	0.845	0.0176	10.656
64	TD-DIP (L)	25.6	0.916	0.0015	0.742	29.0	0.947	0.0107	6.544
64	RED-PSM-ADMM (P)	26.4	0.958	0.0009	0.565	29.3	0.952	0.0054	6.057
128	PSM-TV (R)	26.8	0.912	0.0014	0.782	29.2	0.907	0.0111	9.571
128	TD-DIP (L)	29.0	0.953	0.0010	0.501	32.4	0.953	0.0082	5.100
128	RED-PSM-ADMM (P)	29.9	0.978	0.0006	0.431	33.1	0.972	0.0035	4.723
256	PSM-TV (P)	30.1	0.934	0.0010	0.630	31.9	0.963	0.0068	8.020
256	TD-DIP (L)	31.7	0.966	0.0008	0.445	34.7	0.966	0.0068	4.609
256	RED-PSM-ADMM (P)	33.8	0.987	0.0004	0.315	35.9	0.986	0.0025	4.426

Table 1: Reconstruction accuracies for the time-varying walnut object and compressed material for different  $P$ . Random (R) and ProSep-based (P) initialization are considered for the basis functions of PSM methods. For TD-DIP, average accuracies for the best PSNR reconstruction during optimization are reported assuming such an oracle is available for three different runs. For ease of comparison, parameter configurations for the experiments are provided in Table 3 in Appendix B.

patch-based RED-PSM, and its potential for highly scalable implementation.

$P$	Denoiser	PSNR(dB)	SSIM	MAE	HFEN
256	Full-image	33.8	0.987	0.0004	0.315
256	Patch-based	33.7	0.989	0.0004	0.348
(a) Walnut					
256	Full-image	35.9	0.986	0.0025	4.426
256	Patch-based	35.6	0.981	0.0027	4.559
(b) Compressed object					

Table 2: Performance comparison for different denoiser types for RED-PSM-ADMM. Patch-based denoisers also use DnCNN architecture and have the same configuration and training policy as the full image denoiser. Their patch size is  $8 \times 8$  with a stride of 2. Parameter configurations for the experiments are provided in Table 4 in Appendix B.

**Acknowledgements.** We thank Dr. Brian M. Patterson for providing the data for the compressed material experiments.

## Appendix

### A. PSNR vs. $t$ Comparisons

In Figure 7, PSNR (in dB) values of reconstructed frames at each  $t$  are shown for every method when  $P = 256$  for both objects. TD-DIP results show the region between the best and the worst PSNR values for each frame for three different runs to highlight the varying performance. RED-PSM provides consistently better PSNR values for all  $t$  compared to the best TD-DIP performance for the warped walnut object. It also overperforms the best TD-DIP re-



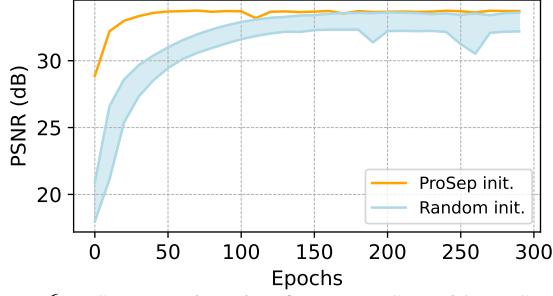


Figure 6: PSNR vs. iteration for RED-PSM with ProSep and random initialization as described in Section 5.3 for the dynamic walnut object with  $P = 256$  and other parameters as described in Table 3 in Appendix B. To highlight the varying performances of five different runs with random initialization, the area between the best and the worst PSNR for each epoch is filled with blue color.

constructed frames in the significant majority of  $t$  for the compressed object. As expected, PSM-TV is suboptimal to other compared methods. These figures also show the transient behavior for all methods at the beginning and the end of the motion for both objects.

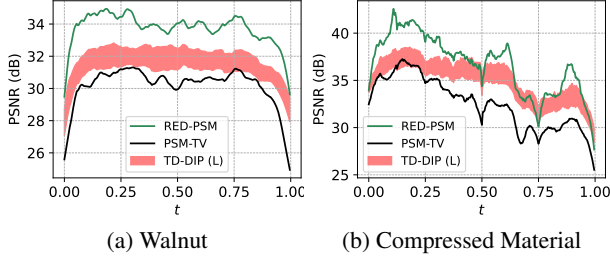


Figure 7: Reconstruction PSNR vs time for the (a) time-varying walnut, and (b) compressed material object (Right) using different methods for  $P = 256$ . To highlight the varying performances of three runs with TD-DIP, the area between the best and the worst PSNR for each  $t$  is filled with red.

## B. Experimental configurations

In Table 3, PSM-TV and PSM-RED-ADMM parameter selections for the experiments listed in Table 1 are provided. Likewise, Table 4 shows the parameter configurations for the denoiser type comparison experiments for RED in Table 2. On the other hand, Table 5 contains the architectural information for the DnCNN denoisers used for the two different object types throughout this work.

## C. Convergence analysis for RED-PSM-ADMM

In this analysis, a simple spatial basis regularization term  $\frac{\chi}{2}\|\Lambda\|_F^2$  is added to the objective in (3). This results, as shown below, in the boundedness of the iterates

		(a) Walnut				(b) Comp. Material			
$P$	Method	$K$	$d$	$\lambda$	$\beta$	$K$	$d$	$\lambda$	$\beta$
32	PSM-TV (R)	3	4	5e-2	-	3	4	10	-
32	PSM-RED-ADMM (P)	3	7	1e-4	1e-4	3	9	5.12e-2	1.6e-2
64	PSM-TV (R)	3	4	5e-2	-	5	6	10	-
64	PSM-RED-ADMM (P)	4	7	1e-4	5e-4	5	9	32e-4	4e-3
128	PSM-TV (R)	5	7	5e-2	-	8	9	5	-
128	PSM-RED-ADMM (P)	6	9	2e-4	2e-4	8	11	4e-4	2e-3
256	PSM-TV (P)	10	11	5e-2	-	11	13	10	-
256	PSM-RED-ADMM (P)	10	11	5e-5	1e-4	11	13	1e-4	1e-3

Table 3: The parameter configurations for the reconstruction accuracies for the complete 3D time-varying objects for different  $P$  in Table 1. The latent temporal penalty weight is selected as  $\xi = 10^{-1}$  for the walnut, and  $\xi = 10^{-3}$  for the compressed object experiments.

		(a) Walnut				(b) Comp. Material			
$P$	Denoiser	$K$	$d$	$\lambda$	$\beta$	$K$	$d$	$\lambda$	$\beta$
256	Full-image	10	11	5e-5	1e-4	11	13	1e-4	1e-3
256	Patch-based	10	11	5e-5	1e-4	11	13	1e-4	1e-3

Table 4: The proposed method parameter configurations for the denoiser type study experiments in Table 2.

Dataset	# of layers	# of channels	Denoising
Walnut	6	64	Direct
Comp. material	3	32	Residual

Table 5: Denoiser DnCNN configurations for the synthetically warped walnut and compressed object datasets.

$(f^{(i)}, \Lambda^{(i)}, \Psi^{(i)})$ . The weight  $\chi > 0$  can be chosen small enough to make the deviation of the solution from the one without this penalty negligible.<sup>3</sup>

As mentioned in Section 4.4, our analysis follows the steps of [9] closely. However, different to [9], our objective function includes factorized terms in bilinear form. Furthermore, our analysis includes a proof (similar to [30]) of the boundedness of the iterates to justify the existence of points of accumulation of the iterate sequence, which appears to have been inadvertently left out in [9].

The optimization problem is

$$\min_{f, \Lambda, \Psi} H(f, \Lambda, \Psi) \quad \text{s.t.} \quad f = \Lambda \Psi^T \quad (13)$$

$$\text{where} \quad H(f, \Lambda, \Psi) = \|\bar{R}\Lambda\Psi^T - g\|_F^2 + \lambda D(f) + \chi \|\Lambda\|_F^2 + \xi \|\Psi\|_F^2. \quad (14)$$

The Lagrangian function with dual variable  $\gamma$  is given by

$$\begin{aligned} \mathcal{L}[\Lambda, \Psi, f; \gamma] = & \|\bar{R}\Lambda\Psi^T - g\|_F^2 + \lambda D(f) \\ & + \frac{\chi}{2} \|\Lambda\|_F^2 + \frac{\xi}{2} \|\Psi\|_F^2 + \langle \gamma, (\Lambda\Psi^T - f) \rangle, \end{aligned} \quad (15)$$

<sup>3</sup>Alternatively, instead of the Frobenius norm penalty, an indicator function for  $\|\Lambda\|_F$  with an appropriate bound can be added to the objective, achieving coercivity without affecting the solution at all. However, this makes the analysis, although tractable, more involved due to the non-differentiability of the objective with respect to  $\Lambda$ , and is therefore avoided in this paper.

where the inner product is defined as  $\langle A, B \rangle = \text{Tr}(A^T B)$ , and  $\bar{R} : \mathbb{R}^{J^2 \times P} \rightarrow \mathbb{R}^{J \times P}$  is the operator computing a projection at view angle  $\theta_t$  of the snapshot at time  $t$ ,  $t = 1, \dots, P$  of the dynamic image  $\Lambda \Psi^T$ , i.e., of the column indexed by  $t$  of  $\Lambda \Psi^T$ . In other words, it performs  $R_{\theta_t}(\sum_k \Lambda_k \psi_k[t])$  for each  $t$ .

The corresponding augmented Lagrangian is

$$\begin{aligned} \mathcal{L}_\beta[\Lambda, \Psi, f; \gamma] &= \|\bar{R}\Lambda\Psi^T - g\|_F^2 + \lambda D(f) \\ &+ \frac{\chi}{2} \|\Lambda\|_F^2 + \frac{\xi}{2} \|\Psi\|_F^2 + \langle \gamma, (\Lambda\Psi^T - f) \rangle + \frac{\beta}{2} \|\Lambda\Psi^T - f\|_F^2. \end{aligned} \quad (16)$$

The bilinear ADMM algorithm for this augmented Lagrangian is Algorithm 3.

---

**Algorithm 3** PSM-ADMM with  $\ell_2$ -norm penalty for  $\Lambda$ .

---

**input:**  $\Lambda^{(0)}, \Psi^{(0)}, \gamma^{(0)}, f^{(0)} = \Lambda^{(0)}\Psi^{(0)T}, \beta > 0, \lambda > 0, \xi > 0$

- 1: **for**  $i \in \{1, \dots, I\}$  **do**
- 2:  $\Lambda^{(i)} = \arg \min_{\Lambda} S_\Lambda(\Lambda, \Psi^{(i-1)}, f^{(i-1)}, \gamma^{(i-1)})$   
 $S_\Lambda = \|\bar{R}\Lambda\Psi^{(i-1)T} - g\|_F^2 + \frac{\chi}{2} \|\Lambda\|_F^2$   
 $+ \frac{\beta}{2} \|\Lambda\Psi^{(i-1)T} - f^{(i-1)} + \frac{1}{\beta}\gamma^{(i-1)}\|_F^2$
- 3:  $\Psi^{(i)} = \arg \min_{\Psi} S_\Psi(\Lambda^{(i)}, \Psi, f^{(i-1)}, \gamma^{(i-1)})$   
 $S_\Psi = \|\bar{R}\Lambda^{(i)}\Psi^T - g\|_F^2 + \frac{\xi}{2} \|\Psi\|_F^2$   
 $+ \frac{\beta}{2} \|\Lambda^{(i)}\Psi^T - f^{(i-1)} + \frac{1}{\beta}\gamma^{(i-1)}\|_F^2$
- 4:  $f^{(i)} = \arg \min_f S_f(\Lambda^{(i)}, \Psi^{(i)}, f, \gamma^{(i-1)})$   
 $S_f = \lambda D(f) + \frac{\beta}{2} \|\Lambda^{(i)}\Psi^{(i)T} - f + \frac{1}{\beta}\gamma^{(i-1)}\|_F^2$
- 5:  $\gamma^{(i)} = \gamma^{(i-1)} + \beta(\Lambda^{(i)}\Psi^{(i)T} - f^{(i)})$
- 6: **end for**

---

Algorithm 3 will be shown in Theorem 1 to converge to a stationary point of Problem (13), which is defined below.

**Definition 1 (Stationary solution for Problem (13)).**

Let  $\gamma$  be the dual variable associated with the constraint  $f = \Lambda\Psi^T$ . Then the point  $W^* = (\Lambda^*, \Psi^*, f^*, \gamma^*)$  is a stationary solution of the problem (13) if it satisfies the stationarity and primal feasibility conditions for the variables of the Lagrangian in (15):

$$\nabla_f \mathcal{L}(\Lambda^*, \Psi^*, f^*; \gamma^*) = \lambda \nabla D(f^*) - \gamma^* = 0; \quad (17a)$$

$$\begin{aligned} \nabla_\Lambda \mathcal{L}(\Lambda^*, \Psi^*, f^*; \gamma^*) &= (2\bar{R}^T(\bar{R}\Lambda^*\Psi^{*T} - g) + \gamma^*)\Psi^* \\ &+ \chi\Lambda^* = 0; \end{aligned} \quad (17b)$$

$$\begin{aligned} \nabla_\Psi \mathcal{L}(\Lambda^*, \Psi^*, f^*; \gamma^*) &= (2\bar{R}^T(\bar{R}\Lambda^*\Psi^{*T} - g) + \gamma^*)^T \Lambda^* \\ &+ \xi\Psi^* = 0; \end{aligned} \quad (17c)$$

$$f^* = (\Lambda\Psi^T)^{(*)}. \quad (17d)$$

By its definition, a stationary solution of (13) satisfies the necessary first-order conditions for optimality.

To state Theorem 1, we need to introduce some additional definitions pertaining to the denoiser  $G$  used in RED.

**Definition 2 (Local Homogeneity [27]).** A function  $G : \mathbb{R}^n \rightarrow \mathbb{R}^n$  is locally homogeneous if  $G(cf) = cG(f)$  for any  $c \in \mathbb{R}$  satisfying  $|c - 1| \leq \epsilon$  for sufficiently small  $\epsilon > 0$ .

Local homogeneity of  $G$  leads to the identity  $\nabla_f G(f)f = G(f)$ , where  $\nabla_f G(f)$  is the Jacobian of  $G$  [27], which in combination with (4) yields the gradient rule of RED in (7).

**Definition 3 (Strong Passivity [27]).** A function  $G$  is strongly passive if  $\|G(f)\| \leq \|f\|$ .

**Theorem 1.** Suppose that the denoiser  $G_\phi$  is locally homogeneous,  $L_G$  Lipschitz continuous, and strongly passive.

Then, if  $\beta > 2L$  where  $L \triangleq \lambda(1 + L_G)$ , Algorithm 3 converges globally (i.e., regardless of initialization) to a stationary solution  $(f^*, \Lambda^*, \Psi^*)$  of (13) in the following sense:

- (i) The sequence of values of the objective  $H$  converges to a limit  $H^* = H(f^*, \Lambda^*, \Psi^*)$ ; and
- (ii) The iterates generated by Algorithm 3 converge subsequentially to a stationary solution  $(f^*, \Lambda^*, \Psi^*, \gamma^*)$  of (13), that is, any accumulation point (of which there is at least one) of the sequence  $(f^{(i)}, \Lambda^{(i)}, \Psi^{(i)}, \gamma^{(i)})$  is a stationary solution of (13).

**Proof of Theorem 1.** We first establish some simple consequences of the assumed properties of the denoiser. First, the objective  $H(f, \Lambda, \Psi)$  (14) is lower bounded by  $\underline{H} \in \mathbb{R}$  because the RED regularizer  $D(f)$  is non-negative, as follows from the strong passivity assumption on  $G_\phi$ ,

$$\begin{aligned} D(f) &= f^T(f - G_\phi(f)) = \|f\|_F^2 - f^T G_\phi(f) \\ &\geq \|f\|_F^2 - \|f\|_F \|G_\phi(f)\|_F \geq 0. \end{aligned} \quad (18)$$

Second, we have the following result.

**Lemma 2.** If the denoiser  $G_\phi$  is locally homogeneous and  $L_G$  Lipschitz continuous, then the regularizer  $D(f)$  is gradient Lipschitz continuous with gradient Lipschitz constant  $L_{\nabla D} = 1 + L_G$ .

*Proof.* By the gradient rule of  $D$  (7) (which is due to the local homogeneity assumption for  $G_\phi$ ), and the assumed  $L_G$  Lipschitz continuity of the denoiser  $G_\phi$  we have

$$\begin{aligned} \|\nabla D(f_1) - \nabla D(f_2)\|_F &= \|f_1 - f_2 - (G_\phi(f_1) - G_\phi(f_2))\|_F \\ &\leq \|f_1 - f_2\|_F + \|G_\phi(f_1) - G_\phi(f_2)\|_F \\ &\leq (1 + L_G)\|f_1 - f_2\|_F. \end{aligned}$$

□

Third, we establish strong convexity of the objectives in the different subproblems in Algorithm 3. Clearly, for any choice of positive constants  $\xi$  and  $\chi$  the objectives  $S_\Lambda$  and  $S_\Psi$  in the subproblems for  $\Lambda$  and  $\Psi$  are strongly convex with moduli  $\alpha_\Lambda \geq \chi$  and  $\alpha_\Psi \geq \xi$ , respectively.

As we show next, with the assumed  $\beta > L$ , the objective  $S_f$  is strongly convex too with modulus  $\alpha_f \geq \beta - L > 0$ . To prove this, we rewrite  $S_f = \rho(f) + \frac{1}{2}(\beta - L)f^T f$  where

$$\begin{aligned} \rho(f) \triangleq & \lambda D(f) + \frac{L}{2} \|f\|_F^2 - \langle f, \beta \Lambda^{(i)} \Psi^{(i)T} + \gamma^{(i-1)} \rangle \\ & + \frac{\beta}{2} \|\Lambda^{(i)} \Psi^{(i)T} + \frac{1}{\beta} \gamma^{(i-1)}\|_F^2 \end{aligned}$$

and show that  $\rho(f)$  is a convex function. Since  $\frac{1}{2}(\beta - L)f^T f$  is convex quadratic for  $\beta > L$ , it then follows (by one of the alternative definitions of strong convexity) that  $S_f$  is a strongly convex function with modulus  $\alpha_f \geq \beta - L$ .

All that remains, is to show that  $\rho(f)$  is a convex function. This follows immediately by recalling Lemma 2, that  $\lambda D(f)$  is gradient Lipschitz continuous with gradient Lipschitz constant  $L = \lambda(1 + L_G)$ , and applying Lemma 3 below to the first two terms of  $\rho(f)$ .

**Lemma 3.** (Thm. 2.1 of [39]) *If  $D(f) : \mathbb{R}^n \rightarrow \mathbb{R}$  is Lipschitz continuously differentiable on a convex set  $C$  with some Lipschitz constant  $L$ , then  $\phi(f) = D(f) + \frac{1}{2}\beta f^T f$  is a convex function on  $C$  for every  $\beta \geq L$ .*

With these preliminaries established, our proof of Theorem 1 follows steps similar to [9](Sec. 4.2), but for our own Algorithm 3:

1. Bounding the size of successive differences of the dual variables by those of the primal ones.
2. Showing that  $\mathcal{L}_\beta[f^i, \Lambda^i, \Psi^i; \gamma^i]$ , the augmented Lagrangian, is a lower-bounded decreasing function.
3. Combining the first two steps and showing convergence to a stationary solution.

The following result upper bounds the successive differences of the dual variable by those of the primal.

**Lemma 4.** *Using the update rules in Algorithm 3, the following holds:*

$$\|\gamma^{(i)} - \gamma^{(i-1)}\|_F \leq L \|f^{(i)} - f^{(i-1)}\|_F \quad \forall i \geq 1,$$

where  $L = \lambda(1 + L_G)$ .

*Proof.* Since  $f^{(i)}$  is the optimal solution for Line 4 of Algorithm 3, it should satisfy the optimality condition

$$\begin{aligned} \lambda \nabla D(f^{(i)}) - \gamma^{(i-1)} - \beta(\Lambda \Psi^{(i)T} - f^{(i)}) &= 0 \\ \lambda \nabla D(f^{(i)}) - \gamma^{(i)} &= 0 \end{aligned} \quad (19)$$

where (19) is due to the dual variable update Step 5 in Algorithm 3. Then, using Lemma 2, we have

$$\begin{aligned} \|\gamma^{(i)} - \gamma^{(i-1)}\|_F &= \lambda \|\nabla D(f^{(i)}) - \nabla D(f^{(i-1)})\|_F \\ &\leq \lambda(1 + L_G) \|f^{(i)} - f^{(i-1)}\|_F \\ &= L \|f^{(i)} - f^{(i-1)}\|_F, \end{aligned}$$

□

Next, using Lemma 4, we show that the augmented Lagrangian is decreasing and bounded below.

**Lemma 5.** *In Algorithm 3, if  $\beta > 2L$ , then the following two propositions hold true.*

1. *Successive differences of the augmented Lagrangian function (16) are bounded above by*

$$\begin{aligned} \mathcal{L}_\beta[f^{(i)}, \Lambda^{(i)}, \Psi^{(i)}; \gamma^{(i)}] - \mathcal{L}_\beta[f^{(i-1)}, \Lambda^{(i-1)}, \Psi^{(i-1)}; \gamma^{(i-1)}] \\ \leq -C_f \|f^{(i)} - f^{(i-1)}\|_F^2 - C_\Psi \|\Psi^{(i)} - \Psi^{(i-1)}\|_F^2 \\ - C_\Lambda \|\Lambda^{(i)} - \Lambda^{(i-1)}\|_F^2, \end{aligned} \quad (20)$$

where  $C_f = \frac{\alpha_f}{2} - \frac{L^2}{\beta}$ ,  $C_\Lambda = \frac{\alpha_\Lambda}{2}$ , and  $C_\Psi = \frac{\alpha_\Psi}{2}$  are positive constants. That is, the augmented Lagrangian is monotone decreasing.

2. *There exists an  $\underline{\mathcal{L}}_\beta$  such that*

$$\mathcal{L}_\beta[f^{(i)}, \Lambda^{(i)}, \Psi^{(i)}; \gamma^{(i)}] \geq \underline{\mathcal{L}}_\beta.$$

That is, the augmented Lagrangian is lower bounded.

*Proof. Part 1.*

For conciseness define  $W^{(i)} = (\Psi^{(i)}, \Lambda^{(i)}, f^{(i)}; \gamma^{(i)})$ . Then the successive difference of the augmented Lagrangian can be expressed by adding and subtracting the term  $\mathcal{L}_\beta[\Psi^{(i)}, \Lambda^{(i)}, f^{(i)}; \gamma^{(i-1)}]$ ,

$$\begin{aligned} \mathcal{L}_\beta[W^{(i)}] - \mathcal{L}_\beta[W^{(i-1)}] \\ = \mathcal{L}_\beta[W^{(i)}] - \mathcal{L}_\beta[\Psi^{(i)}, \Lambda^{(i)}, f^{(i)}; \gamma^{(i-1)}] \\ + \mathcal{L}_\beta[\Psi^{(i)}, \Lambda^{(i)}, f^{(i)}; \gamma^{(i-1)}] - \mathcal{L}_\beta[W^{(i-1)}]. \end{aligned} \quad (21)$$

For the first two terms on the RHS, using Lemma 4 we have

$$\begin{aligned} \mathcal{L}_\beta[W^{(i)}] - \mathcal{L}_\beta[\Psi^{(i)}, \Lambda^{(i)}, f^{(i)}; \gamma^{(i-1)}] \\ = \langle \gamma^{(i)} - \gamma^{(i-1)}, (\Lambda \Psi^T)^{(i)} - f^{(i)} \rangle \\ = \frac{1}{\beta} \|\gamma^{(i)} - \gamma^{(i-1)}\|_F^2 \leq \frac{L^2}{\beta} \|f^{(i)} - f^{(i-1)}\|_F^2. \end{aligned} \quad (22)$$

where the first equality in (22) follows from the dual variable update in Step (5) of Algorithm 3. The last two terms on the RHS of (21) are further split into

$$\begin{aligned} \mathcal{L}_\beta[\Psi^{(i)}, \Lambda^{(i)}, f^{(i)}; \gamma^{(i-1)}] - \mathcal{L}_\beta[W^{(i-1)}] \\ = \mathcal{L}_\beta[\Psi^{(i)}, \Lambda^{(i)}, f^{(i)}; \gamma^{(i-1)}] \\ - \mathcal{L}_\beta[\Psi^{(i)}, \Lambda^{(i)}, f^{(i-1)}; \gamma^{(i-1)}] \\ + \mathcal{L}_\beta[\Psi^{(i)}, \Lambda^{(i)}, f^{(i-1)}; \gamma^{(i-1)}] \\ - \mathcal{L}_\beta[\Psi^{(i-1)}, \Lambda^{(i)}, f^{(i-1)}; \gamma^{(i-1)}] \\ + \mathcal{L}_\beta[\Psi^{(i-1)}, \Lambda^{(i)}, f^{(i-1)}; \gamma^{(i-1)}] - \mathcal{L}_\beta[W^{(i-1)}] \end{aligned} \quad (23)$$

The first two terms on the RHS of (23) are upper bounded using the strong convexity of  $S_f$  with modulus  $\alpha_f$ :

$$\begin{aligned} \mathcal{L}_\beta[\Psi^{(i)}, \Lambda^{(i)}, f^{(i)}; \gamma^{(i-1)}] - \mathcal{L}_\beta[\Psi^{(i)}, \Lambda^{(i)}, f^{(i-1)}; \gamma^{(i-1)}] \\ \leq \langle \nabla_f S_f[\Psi^{(i)}, \Lambda^{(i)}, f^{(i)}; \gamma^{(i-1)}], f^{(i)} - f^{(i-1)} \rangle \\ - \frac{\alpha_f}{2} \|f^{(i-1)} - f^{(i)}\|_F^2 \\ = -\frac{\alpha_f}{2} \|f^{(i-1)} - f^{(i)}\|_F^2, \end{aligned} \quad (24)$$

where the last line of (24) is due to the optimality condition of Line 4 of Algorithm 3 for  $f^{(i)}$ .

The next two terms on the RHS of (23) are upper bounded using the strong convexity of  $S_\Psi$  with modulus  $\alpha_\Psi$  as

$$\begin{aligned} \mathcal{L}_\beta[\Psi^{(i)}, \Lambda^{(i)}, f^{(i-1)}; \gamma^{(i-1)}] - \mathcal{L}_\beta[\Psi^{(i-1)}, \Lambda^{(i)}, f^{(i-1)}; \gamma^{(i-1)}] \\ = S_\Psi(\Lambda^{(i)}, \Psi^{(i)}, f^{(i-1)}; \gamma^{(i-1)}) \\ - S_\Psi(\Lambda^{(i)}, \Psi^{(i-1)}, f^{(i-1)}; \gamma^{(i-1)}) \\ \leq \langle \nabla_\Psi S_\Psi[\Psi^{(i)}, \Lambda^{(i)}, f^{(i-1)}; \gamma^{(i-1)}], \Psi^{(i)} - \Psi^{(i-1)} \rangle \\ - \frac{\alpha_\Psi}{2} \|\Psi^{(i)} - \Psi^{(i-1)}\|_F^2 \\ = -\frac{\alpha_\Psi}{2} \|\Psi^{(i)} - \Psi^{(i-1)}\|_F^2. \end{aligned}$$

Repeating similar steps for the last two terms on the RHS of (23) using the objective  $S_\Lambda$  in Line 2 leads to the upper bound of  $-\frac{\alpha_\Lambda}{2} \|\Lambda^{(i)} - \Lambda^{(i-1)}\|_F^2$ .

Finally, we establish the positivity of the constants in (20). We trivially have  $c_\Psi = \alpha_\Psi \geq \xi > 0$  and  $c_\Lambda = \alpha_\Lambda \geq \chi > 0$ . Next, because  $\alpha_f \geq \beta - L$ , we have  $C_f = \frac{\alpha_f}{2} - \frac{L^2}{\beta} \geq \frac{\beta-L}{2} - \frac{L^2}{\beta} > 0$ , where the last inequality follows by the assumption  $\beta > 2L$ .

Combining these results, we achieve the inequality in (20), which concludes Part 1.

**Part 2.** For Part 2, we need to show that the augmented Lagrangian is lower bounded.

$$\begin{aligned} L_\beta[W^{(i)}] &= H(f^{(i)}, \Lambda^{(i)}, \Psi^{(i)}) \\ &\quad + \langle \gamma^{(i)}, (\Lambda \Psi^T)^{(i)} - f^{(i)} \rangle \\ &\quad + \frac{\beta}{2} \|(\Lambda \Psi^T)^{(i)} - f^{(i)}\|_F^2 \end{aligned} \quad (25)$$

$$\begin{aligned} &\geq H(f^{(i)}, \Lambda^{(i)}, \Psi^{(i)}) \\ &\quad + \langle \lambda \nabla D(f^{(i)}), (\Lambda \Psi^T)^{(i)} - f^{(i)} \rangle \\ &\quad + \frac{L}{2} \|(\Lambda \Psi^T)^{(i)} - f^{(i)}\|_F^2 \end{aligned} \quad (26)$$

$$\geq H(f^{(i)}, \Lambda^{(i)}, \Psi^{(i)}) \quad (27)$$

$$\begin{aligned} &\quad + \lambda D((\Lambda \Psi^T)^{(i)}) - \lambda D(f^{(i)}) \\ &= H(\Lambda^{(i)} \Psi^{(i)T}, \Lambda^{(i)}, \Psi^{(i)}). \end{aligned} \quad (28)$$

where (26) follows by using (19) to replace the second term of (25) by that of (26) and assuming  $\beta > L$ , and (27) is due

to the gradient Lipschitz continuity of the regularizer  $D(\cdot)$ ,

$$\begin{aligned} \lambda D(\Lambda \Psi^T) &\leq \lambda D(f) + \langle \lambda \nabla_f D(f), \Lambda \Psi^T - f \rangle \\ &\quad + \frac{L}{2} \|\Lambda \Psi^T - f\|_F^2. \end{aligned}$$

Then, since we initially showed that our minimization objective in (14) is lower bounded by  $\underline{H}$ , we have

$$H(\Lambda^{(i)} \Psi^{(i)T}, \Lambda^{(i)}, \Psi^{(i)}) \geq \underline{H},$$

which leads, by combining with (28), to  $L_\beta[W^{(i)}] \geq \underline{\mathcal{L}}_\beta = \underline{H}$  and completes the proof of Lemma 5.  $\square$

By Lemma 5, the sequence  $L_\beta[W^{(i)}]$  of augmented Lagrangian values converges. What remains is to address the convergence of the objective  $H$  and of the sequence of iterates  $(f^{(i)}, \Lambda^{(i)}, \Psi^{(i)}, \gamma^{(i)})$  itself to a stationary solution of (13), which we do in the third and final step of the proof of Theorem 1. We start by showing that the duality gap shrinks to zero.

**Lemma 6.** Consider Algorithm 3 for solving problem (13). If  $\beta > 2L$ , then the duality gap goes to zero, i.e.

$$\lim_{i \rightarrow \infty} \|(\Lambda \Psi^T)^{(i)} - f^{(i)}\|_F \rightarrow 0.$$

*Proof.* Lemma 5 implies that when  $\beta > 2L$ , the sequence of augmented Lagrangian values is convergent. Thus, the LHS of (20) converges to zero. This also means that each of the norms on the RHS converges to zero to satisfy the inequality. Hence, the following successive differences converge to zero,

$$f^{(i)} - f^{(i-1)} \rightarrow 0; \Lambda^{(i)} - \Lambda^{(i-1)} \rightarrow 0; \Psi^{(i)} - \Psi^{(i-1)} \rightarrow 0.$$

Furthermore, applying Lemma 4,

$$\gamma^{(i)} - \gamma^{(i-1)} \rightarrow 0.$$

Finally, using the update equation for the dual variable  $\gamma$ , we obtain

$$(\Lambda \Psi^T)^{(i)} - f^{(i)} \rightarrow 0, \quad (29)$$

which completes the proof of Lemma 6.  $\square$

It follows from Lemma 6 that the gap  $L_\beta[W^{(i)}] - H(\Lambda^{(i)} \Psi^{(i)T}, \Lambda^{(i)}, \Psi^{(i)})$  between the augmented Lagrangian and the objective converges to zero, and therefore thanks to the convergence of  $L_\beta[W^{(i)}]$ , the objective  $H$  too converges. This establishes Part (i) of Theorem 1.

Turning to Part (ii) of Theorem 1, we first show that the iterates are bounded.

**Lemma 7.** The iterates  $(f^{(i)}, \Lambda^{(i)}, \Psi^{(i)}, \gamma^{(i)})$  of Algorithm 3 for solving (13) are bounded for  $i > 0$ .

*Proof.* We use the following facts:

- (F1)  $\mathcal{L}_\beta[W^{(i)}]$  is a non-increasing function as  $i$  increases for all  $i > 0$ , as shown in Lemma 5.
- (F2) The objective  $H(f, \Lambda, \Psi)$  is coercive with respect to the second and the third variables.

It follows from (F1) that  $\mathcal{L}_\beta[W^{(i)}] \leq \mathcal{L}_\beta[W^{(0)}]$ ,  $\forall i \geq 0$ . Combining this with (28), yields

$$H((\Lambda\Psi^T)^{(i)}, \Lambda^{(i)}, \Psi^{(i)}) \leq \mathcal{L}_\beta[W^{(i)}] \leq \mathcal{L}_\beta[W^{(0)}]. \quad (30)$$

Now, note that by (13), the first variable  $(\Lambda\Psi^T)^{(i)}$  in  $H((\Lambda\Psi^T)^{(i)}, \Lambda^{(i)}, \Psi^{(i)})$  only appears as the argument of  $D(\cdot)$ , and by (18)  $D(\cdot) \geq 0$ . This implies by (F2) that  $H((\Lambda\Psi^T)^{(i)}, \Lambda^{(i)}, \Psi^{(i)})$  is coercive with respect to  $\Lambda^{(i)}$  and  $\Psi^{(i)}$ . Combining this with the boundedness of  $H$  in (30) implies the boundedness of these iterates.

Next, the boundedness of  $f^{(i)}$  follows from Lemma 6, since we showed that  $\Lambda^{(i)}$  and  $\Psi^{(i)}$ , thus  $(\Lambda\Psi^T)^{(i)}$  are all bounded, and the duality gap shrinks to zero as the iterates progress.

Finally, since all the primary variables are bounded, the augmented Lagrangian is bounded both from below (by Part 2 of Lemma 5) and from above by (30), and the dual variable iterates  $\gamma^{(i)}$  appear only in the linear Lagrangian term, they are also bounded.

This concludes the proof of Lemma 7.  $\square$

It follows that the sequences of iterates  $\{f^{(i)}, \Lambda^{(i)}, \Psi^{(i)}, \gamma^{(i)}\}$  has at least one accumulation point  $(f^*, \Lambda^*, \Psi^*, \gamma^*)$ . Next, we establish the properties of all such accumulation points.

Taking the limit over  $i$  in (19) yields (17a).

Next, since  $\Lambda^{(i)}$  is optimal for the subproblem in Line 2 of Algorithm 3, we have

$$\begin{aligned} \nabla_\Lambda S_\Lambda(\Psi^{(i-1)}, \Lambda^{(i)}, f^{(i-1)}; \gamma^{(i-1)}) &= 0 \\ 2\bar{R}^T(\bar{R}\Lambda^{(i)}\Psi^{(i-1)T}\Psi^{(i-1)} - g\Psi^{(i-1)}) \\ + \beta(\Lambda^{(i)}\Psi^{(i-1)T} - f^{(i-1)} + \frac{1}{\beta}\gamma^{(i-1)})\Psi^{(i-1)} + \chi\Lambda^{(i)} &= 0 \end{aligned}$$

Taking the limit over  $i$  yields (17b). Similarly, taking the limit in the optimality condition with respect to  $\Psi^{(i)}$ ,  $\nabla_\Psi S_\Psi(\Psi^{(i)}, \Lambda^{(i-1)}, f^{(i-1)}; \gamma^{(i-1)}) = 0$  yields (17c). Finally, taking the limit with respect to  $i$  in (29) verifies (17d). These results complete the proof of Theorem 1.  $\square$

## References

- [1] Piecewise Affine Transformation. [https://scikit-image.org/docs/dev/auto\\_examples/transform/plot\\_piecewise\\_affine.html](https://scikit-image.org/docs/dev/auto_examples/transform/plot_piecewise_affine.html).

- [2] In Michael Reed and Barry Simon, editors, *Methods of Modern Mathematical Physics*. Academic Press, 1972.
- [3] Abdul Haseeb Ahmed, Qing Zou, Prashant Nagpal, and Mathews Jacob. Dynamic imaging using deep bi-linear unsupervised representation (deblur). *IEEE transactions on medical imaging*, 41(10):2693–2703, 2022.
- [4] Stephen Boyd, Neal Parikh, Eric Chu, Borja Peleato, Jonathan Eckstein, et al. Distributed optimization and statistical learning via the alternating direction method of multipliers. *Foundations and Trends® in Machine learning*, 3(1):1–122, 2011.
- [5] Ibrahim Danad, Jackie Szymonifka, Joshua Schulman-Marcus, and James K. Min. Static and dynamic assessment of myocardial perfusion by computed tomography. *European Heart Journal - Cardiovascular Imaging*, 17(8):836–844, 03 2016.
- [6] Henri Der Sarkissian, Felix Lucka, Maureen van Eijnatten, Giulia Colacicco, Sophia Bethany Coban, and Kees Joost Batenburg. A cone-beam x-ray computed tomography data collection designed for machine learning. *Scientific data*, 6(1):215, 2019.
- [7] Jonathan Eckstein and Dimitri P Bertsekas. On the Douglas–Rachford splitting method and the proximal point algorithm for maximal monotone operators. *Mathematical Programming*, 55(1):293–318, 1992.
- [8] Daniel Gabay and Bertrand Mercier. A dual algorithm for the solution of nonlinear variational problems via finite element approximation. *Computers & mathematics with applications*, 2(1):17–40, 1976.
- [9] Davood Hajinezhad and Qingjiang Shi. Alternating direction method of multipliers for a class of nonconvex bilinear optimization: convergence analysis and applications. *Journal of Global Optimization*, 70:261–288, 2018.
- [10] Justin P. Haldar and Zhi-Pei Liang. Spatiotemporal imaging with partially separable functions: A matrix recovery approach. In *2010 IEEE International Symposium on Biomedical Imaging: From Nano to Macro*, pages 716–719, April 2010.
- [11] Berk Iskender, Yoram Bresler, and Marc L Klasky. Dynamic tomography reconstruction by projection-domain separable modeling. In *2022 IEEE 14th Image, Video, and Multidimensional Signal Processing Workshop (IVMSP)*, pages 1–5. IEEE, 2022.
- [12] Berk Iskender, Marc L Klasky, and Yoram Bresler. Dynamic tomography reconstruction by projection-domain separable modeling. *arXiv:2204.09935*, 2022.
- [13] Clément Jailin and Stéphane Roux. Dynamic tomographic reconstruction of deforming volumes. *Materials*, 11(8), 2018.
- [14] Clément Jailin, Stéphane Roux, David Sarrut, and Simon Rit. Projection-based dynamic tomography. *Physics in Medicine & Biology*, 66(21):215018, 2021.
- [15] Diederik P Kingma and Jimmy Ba. Adam: A method for stochastic optimization. *arXiv preprint arXiv:1412.6980*, 2014.
- [16] Shuli Ma, Huiqian Du, Qiongzhi Wu, and Wenbo Mei. Dynamic MRI reconstruction exploiting partial separability and

- t-SVD. In *2019 IEEE 7th International Conference on Bioinformatics and Computational Biology (ICBCB)*, pages 179–184. IEEE, 2019.
- [17] Shuli Ma, Youchen Fan, and Zhifei Li. Dynamic MRI exploiting partial separability and shift invariant discrete wavelet transform. In *2021 6th International Conference on Image, Vision and Computing (ICIVC)*, pages 242–246. IEEE, 2021.
- [18] Eric Maire, Christophe Le Bourlot, Jérôme Adrien, Andreas Mortensen, and Rajmund Mokso. 20 Hz X-ray tomography during an in situ tensile test. *International Journal of Fracture*, 200(1):3–12, 2016.
- [19] JPB O’Connor, PS Tofts, KA Miles, LM Parkes, G Thompson, and A Jackson. Dynamic contrast-enhanced imaging techniques: CT and MRI. *The British journal of radiology*, 84:S112–S120, 2011.
- [20] Brian M Patterson. Personal communication. 2022.
- [21] Brian M Patterson, Nikolaus L Cordes, Kevin Henderson, Jason J Williams, Tyler Stannard, Sudhanshu S Singh, Angel Rodriguez Ovejero, Xianghui Xiao, Mathew Robinson, and Nikhilesh Chawla. In situ x-ray synchrotron tomographic imaging during the compression of hyperelastic polymeric materials. *Journal of materials science*, 51(1):171–187, 2016.
- [22] Brian M Patterson, Lindsey Kuettner, Trevor Shear, Kevin Henderson, Matthew J Herman, Axinte Ionita, Nikhilesh Chawla, Jason Williams, Tao Sun, Kamel Fezzaa, et al. Synchrotron ct imaging of lattice structures with engineered defects. *Journal of Materials Science*, 55(25):11353–11366, 2020.
- [23] Saiprasad Ravishankar and Yoram Bresler. Mr image reconstruction from highly undersampled k-space data by dictionary learning. *IEEE transactions on medical imaging*, 30(5):1028–1041, 2010.
- [24] Fitsum Reda, Janne Kontkanen, Eric Tabellion, Deqing Sun, Caroline Pantofaru, and Brian Curless. Film: Frame interpolation for large motion. *arXiv preprint arXiv:2202.04901*, 2022.
- [25] Edward T Reehorst and Philip Schniter. Regularization by denoising: Clarifications and new interpretations. *IEEE transactions on computational imaging*, 5(1):52–67, 2018.
- [26] Dirk Robinson and Peyman Milanfar. Fast local and global projection-based methods for affine motion estimation. *Journal of Mathematical Imaging and Vision*, 18(1):35–54, 2003.
- [27] Yaniv Romano, Michael Elad, and Peyman Milanfar. The little engine that could: Regularization by denoising (red). *SIAM Journal on Imaging Sciences*, 10(4):1804–1844, 2017.
- [28] Michael Salerno, Behzad Sharif, Håkan Arheden, Andreas Kumar, Leon Axel, Debiao Li, and Stefan Neubauer. Recent advances in cardiovascular magnetic resonance: techniques and applications. *Circulation: Cardiovascular Imaging*, 10(6):e003951, 2017.
- [29] Alessio Scanziani, Kamaljit Singh, Tom Bultreys, Branko Bijeljic, and Martin J Blunt. In situ characterization of immiscible three-phase flow at the pore scale for a water-wet carbonate rock. *Advances in Water Resources*, 121:446–455, 2018.
- [30] Yu Wang, Wotao Yin, and Jinshan Zeng. Global convergence of admm in nonconvex nonsmooth optimization. *Journal of Scientific Computing*, 78:29–63, 2019.
- [31] Zhou Wang, Alan C Bovik, Hamid R Sheikh, and Eero P Simoncelli. Image quality assessment: from error visibility to structural similarity. *IEEE transactions on image processing*, 13(4):600–612, 2004.
- [32] N.P. Willis and Y. Bresler. Optimal scan for time-varying tomography. II. Efficient design and experimental validation. *IEEE Transactions on Image Processing*, 4(5):654–666, 1995.
- [33] P.N. Willis and Y. Bresler. Optimal scan for time-varying tomography. I. Theoretical analysis and fundamental limitations. *IEEE Transactions on Image Processing*, 4(5):642–653, 1995.
- [34] Xiong Xiong and Kaihuai Qin. Linearly estimating all parameters of affine motion using radon transform. *IEEE Transactions on Image Processing*, 23(10):4311–4321, 2014.
- [35] Jaejun Yoo. Time-Dependent Deep Image Prior for Dynamic MRI. <https://github.com/jaejun-yoo/TDDIP>, 2021.
- [36] Jaejun Yoo, Kyong Hwan Jin, Harshit Gupta, Jerome Yerly, Matthias Stuber, and Michael Unser. Time-dependent deep image prior for dynamic mri. *IEEE Transactions on Medical Imaging*, 40(12):3337–3348, 2021.
- [37] Kai Zhang, Wangmeng Zuo, Yunjin Chen, Deyu Meng, and Lei Zhang. Beyond a gaussian denoiser: Residual learning of deep cnn for image denoising. *IEEE transactions on image processing*, 26(7):3142–3155, 2017.
- [38] Bo Zhao, Justin P Haldar, Anthony G Christodoulou, and Zhi-Pei Liang. Image reconstruction from highly undersampled (k, t)-space data with joint partial separability and sparsity constraints. *IEEE transactions on medical imaging*, 31(9):1809–1820, 2012.
- [39] Sanjo Zlobec. On the liu–floudas convexification of smooth programs. *Journal of Global Optimization*, 32(3):401–407, 2005.
- [40] Qing Zou, Abdul Haseeb Ahmed, Prashant Nagpal, Stanley Kruger, and Mathews Jacob. Dynamic imaging using a deep generative storm (gen-storm) model. *IEEE transactions on medical imaging*, 40(11):3102–3112, 2021.